Chapter 5

Title: Room-Temperature Stabilized α-Sn Nanocrystals for *in-vivo* Toxicology Evaluation and photothermal therapy Corroborated by FFT Modelling

5.1 Introduction

Tin (Sn) is an exceptional metal that boasts the extraordinary ability to demonstrate an array of distinct properties when subjected to modifications from bulk to Nano level.[296, 297] The structural characteristics of Sn metal offer valuable insight into its fundamental nature, as it is conventionally available in two forms: β-Sn (tetragonal structure) and α-Sn (diamond cubic structure). When the ambient temperature descends beneath the threshold of 13 °C, β-Sn (metallic phase) goes through a phase transition to α-Sn (zero band gap semimetal) accompanied by a volumetric surge.[298, 299] Tin demonstrates optoelectronic properties in both its semi-metallic (gray tin) and metallic states (white tin), and these properties can be manipulated at the Nano-scale contingent upon the size and shape of the intended nanomaterial[297]. Furthermore, tin nanocrystals (Sn NCs) have been the subject of abundant theoretical examinations, disclosing their unparalleled scientific significance,[298, 300-302]which facilitated the fabrication of large β-Sn nanocrystals (>12 nm) [303-306] or to fortify the stability of β-Sn crystals through the use of charged particles [307] or by imbuing them within bulk materials [308] so far.

The synthesis of bulk alpha tin (α-Sn) is fraught with considerable difficulties and impediments. In view of the thermodynamic instability of bulk α-Sn at ambient temperatures[309], the use of a substrate with a matching lattice constant, such as InSb(100), is imperative for the growth of bulk α-Sn as a crystallization seed. An alternative approach for producing bulk α-Sn involves the utilization of molecular beam epitaxy in conjunction with the subsequent 400 °C annealing of thin films over an

InSb(111) matrix.[310]. Similar research has been conducted on silicon wafers (1,0 0) with SiOx coatings (70 nm)[173], CdTe and InSb substrates[309, 311], and amorphous silicon substrates.[312] In the latest scenario, SnGe samples consisting of alloyed β-Sn, were heated at 300-350 ℃ on an oxide layer and silicon substrates, resulting in the formation and growth of α-Sn with their beta phase, as evinced by XRD,[313] all with the intention of generating bulk α-Sn. Moreover, at the nanometer scale, stable ultra-small α-Sn nanocrystals and mixed phases of α/β Sn were fabricated in ethanol solutions through micro-plasma synthesis, since at the nanoscale realm properties are again tuned, which enhances the metastability of ultra-small nanocrystals.[297] In addition, since the Bohr exciton radius (12.5 nm) for α-Sn is much larger than the size of synthesized ultra-small nanocrystals, the semi-metal diamond cubic α-Sn is more vulnerable to quantum confinement, resulting in a widening of its band gap from 0 to 1.25 eV.[301] Furthermore, the utilization of microplasma techniques presents a plethora of benefits for regulating the size of nanoparticles, however, it necessitates an intricate and advanced apparatus as well as elevated gas temperatures (1426 ℃-1726 ℃) during the nanoparticle synthesis[314]. Henceforth, the fabrication of α-Sn nanocrystals in solvent water at ambient temperature appears to be unachievable. The current investigation is thus dedicated to the quest for a substitute procedure, such as a room-temperature synthesis, for the production of α-Sn nanocrystals. Currently, as per our cognizance, the facile synthesis of α-Sn nanocrystals in solvent water at ambient temperature without employing either substrates like InSb, CdTe, and silicon etc. has been deemed to be a great challenge so far. To achieve this, we devised a new strategy based on a reduction technique that allows for the simple fabrication of α-Sn nanocrystals with their beta phase in the solvent water via purging inert gas. We overcome the limitation of α-Sn formation at ambient temperature, which is described as follows: When the synthesis of tin nanocrystals was

first started using a $SnCl_2$ as a precursor and putting a capping agent followed by a reductant in DI water, some black-coloured bit of fluorescent material appeared, which vanished into a transparent colour after three days. Then, a reductant was put drop-wise in standalone DI water, and the colour of the solution changed from black to grey after adding more drops of reductant, and the average size of synthesized nanocrystals was measured to be 4.9 nm through HR-TEM analyses. Then, the nanocrystal lattice fringes were obtained through TEM, XRD, and SAED patterns, and these lattice fringes were found to be of α-Sn with beta forms. And then, the Bohr exciton radius was calculated (12.5 nm) for α-Sn nanocrystals. The synthesized nanocrystals size was 4.9 nm less than the Bohr exciton radius size. Hence, such nanocrystals are found to be stable at room temperature, detected through an increment in band gap from 0 to 2.38 eV for quantum confinement. Ultimately, it overcomes the limitation of α-Sn nanocrystal formation at ambient temperature.

For the comparison of properties and application of Sn nanocrystals with other materials we have provided below table :

Table 1' Comparisom study of Sn nanocrystals with other systems.

Aspect	**Current Synthesis**	**Previous Synthesis**
Stability at Room Temperature	Stable at room temperature	Required substrates for stabilization[482]
Size	Ultrasmall (~4.9 nm)	Dependent on synthesis method
Synthesis Medium	Aqueous (DI water)	Varied (e.g., ethanol[483], diethylene glycol (DEG)[484])
Toxicity	Non-toxic	Typically involve toxic substance lithium and lead substrate[485, 486]
Complexity	Simplified synthesis process	Highly complex setups[483, 487]
Cost	Potentially lower cost	High cost[488]
Substrate Utilization	No bulky substrates required	Dependent on specific bulky substrates[482, 486, 488, 489]
Size Control	Controlled size (~4.9 nm)	Varied (typically greater than 10 nm)[485, 487]
Temperature Requirement	Room temperature	Elevated gas temperatures[483]
Side Effects on Vital Organs (Rats)	No Side-effects	Not mentioned

Photothermal near-infrared (NIR) cancer killing experiments are discussed in the current thesis for several reasons:

Relevance: Photothermal therapy is an emerging and promising approach for the purpose of cancer treatment that has gained a deep insight in recent years. By discussing these experiments, one can address and discuss the various important and relevant points in cancer research.

Non-invasive: Photothermal therapy is typically considered a non-invasive method, reducing the need for surgery and minimizing patient discomfort and it typically involves a quick recovery time in contrast to other surgical methods.

Deep tissue penetration: 980 nm light can easily penetrate tissues deeply without significant damage to healthy cells, and reaches nearby cancer cells located anywhere within the body.

Interestingly, herein we developed tin nanocrystals, which are ultra-small and exhibit broad NIR light absorption (800-1200 nm), which increases consistently with increasing tin concentration up to 1.58 mg/ml. Due to strong NIR Property exhibited by these nanocrystals and eminent photothermal efficiency of 42.8%, these are utilized as a photothermal agent for photothermal experiments. In spite of above, these nano-crystals lie below the size of the kidney filtration upper limit (10 nm) in contrast to conventional used photothermal agents of large sizes with high efficiency. (See below Table 1")

Table 1": Photothermal efficiency of tin nanocrystals (current study) with prior studies.

Photothermal agent (Size)	Photothermal Efficiency
Au Nanoshells[490](150 nm)	15%
Gold Nanorods[491] (> 40 nm)	21.3%
Pt-PEG Nanoworms[492] (100 nm)	38.9%
Pt Nanoparticles[493] (<21 nm)	22.98-30.88%
Pt Cubes [494] (40 nm)	32.3%
Cys-CuS NPs[491] (18nm)	38%
This Work: Sn nanocrystals **(~4.9 nm)**	**42.8%**

5.2 Materials and Methods

5.2.1 Equipment and Materials

X-ray diffraction (XRD) (Bruker, Model-D8 Advance (Eco)) techniques were performed to investigate the phase presence in developed tin nanocrystals. The size and particle distribution were obtained utilizing FEI TECNAI G@ 20 TWIN High -resolution transmission electron microscopy (HR-TEM) with a 200 kV accelerating voltage. The UV-absorbance spectra were carried out using JASCO V-730 spectrophotometer in the spectral range of 280-1100 nm. For Laser power supply MODEL No: PSU-III-LED with input 85-264 VAC, 47-63 Hz, and 2A were utilized. Tin (II) chloride dehydrate GR and Polyethylene glycol 4000 is purchased through MERCK Specialties Private Limited Mumbai, India and Sodium borohydride, Hi-AR^{TM}/ACS ($NaBH_4$) is procured through HIMEDIA. ALT (GPT) and AST (GOT)-Modified IFCC kits were purchased from TARA Clinical Systems, India. ARKRAY Healthcare, Ltd., India provided the MBK Alkaline Phosphatase Assay kit. CK-MB (NAC act.) assay and creatinine kit were procured from coral Clinical Systems, India.

5.2.2 Materials used for *in-vitro* photothermal application:

U-87 MG cell line was procured from NCCS Pune India. DMEM and 12 well cell culture plate were purchased from Genetix Pvt. Ltd. T-25 flask and 96 well plate obtained from Eppendorf. FBS (Fetal Bovine Serum) Trypsin-EDTA and Penicillin-streptomycin were procured from Gibco. PBS (Phosphate Buffer Saline) was prepared in the laboratory.

5.3 Methods

5.3.1 The hypothesis behind the planned protocol in its aim to synthesize α-Sn nanocrystals and their synthesis in deionized water:

The hypothesis is presented below:

- ✓ Novel synthesis method for α-Sn nanocrystals in aqueous phase ((DI water).
- ✓ Avoid use of toxic substances like lithium, lead-telluride for α-Sn synthesis.
- ✓ Achieve room-temperature stability of α-Sn without use of bulky reactive substrates such as Si and InSb.
- ✓ Trying to generate ultra-small α- Sn nanocrystals below the kidney filtration threshold (10 nm).
- ✓ Predict biocompatibility for biomedical use.
- ✓ Harness the NIR absorption of α-Sn nanocrystals for photothermal therapy.

Prior to conducting the experiment, the glassware was thoroughly rinsed using Aqua Regia (HCl: HNO_3 = 3:1 by volume), and subsequently with ethanol and deionized (DI) water. In the nascent stage of the synthesis process, two distinct deionized water samples, measuring 48 ml and 20 ml, were respectively placed in a 250 ml conical flask and a 20 ml beaker. These water samples were then subjected to a purging with nitrogen gas, being streamed at a flow rate of 100 ml/min, for a period of 20 minutes. Next, a solution of

3.69 mM of $SnCl_2$ was prepared in nitrogen-purged water in the conical flask, which was maintained at room temperature, and a magnetic stirrer was set to 500 rpm. Concurrently, another solution of 39.65 mM of $NaBH_4$ was prepared in nitrogen-purged water. This $NaBH_4$ solution was then added dropwise to the $SnCl_2$ solution. Upon adding a few drops of $NaBH_4$, the color of the reaction solution soared from colorless to deep-black. When the addition of $NaBH_4$ progressed in dropwise manner, by introducing approximate 9 ml of its volume, the solution evolved from deep-black into a grayish color, indicating the successful synthesis of alpha tin nanocrystals along with their beta forms. To restrict the growth of tin nanocrystals in the solvent water, PEG 4000 biocompatible polymer was employed at the end of the reaction. The magnetic stirrer was set to 900 rpm to enable effective mixing of the polymer with the tin nanocrystals for a period of 2 hours. After the reaction was completed, any excess polymer and $NaBH_4$ were removed by washing the tin nanocrystals with water through centrifugation at 10,000 rpm. The nanocrystal sample was collected in a 2 ml centrifuge tube for further required characterizations. Finally, the synthesized sample was submitted for ICPMS analysis to determine the concentration of tin nanocrystals in solvent water.

5.3.2 Animals

We used 180±20 g adult albino male Wistar rats (obtained from IMS-BHU, Varanasi, India) as experimental animals. A 25 °C controlled environment and 45–55% relative humidity (12/12 h dark/light cycle) was maintained and the rats were habituated to the laboratory environmental condition for a week. The rats were given food (Paramount Laboratory Animal feed, Lanka, India) and water ad libitum throughout the experimental protocol. As per the NIH (National Institute of Health) guidelines (Publication 85-23, revised 2013), the current study was performed to minimize animal use and the experimental protocol approved by the Institute's Animal Ethical Committee of Indian

Institute of Technology (Banaras Hindu University) Regd. No. 2123/GO/Re/S/21/CPCSEA, IAEC Approval Number: IIT(BHU)/IAEC/2022/075.

5.3.3 *In-vivo* acute toxicity study:

The *in-vivo* acute tail vein toxicity of tin nanocrystals were performed on the 4 groups of active and healthy adult male Wistar rats. According to the experimental protocol, six rats were randomly assigned to each group and administered a dose similar to doses used in photothermal study to evaluate the safety profile of tin nanocrystals (Q1, Q2, and Q3) in such rats. The tin nanocrystals were suspended in DI water and were administered through the tail vein of rats and were examined every day for 14 days, beginning within the first four hours of their administration for any sign of toxicity. Rats were monitored during the toxicity assessment for changes in, eyes, fur, skin, and subsequent mucous membranes, as well as signs related to convulsions, tremors, lethargy, salivation, diarrhea, sleep, and comatoseness. Further, experimental animals body weight and food consumption was also evaluated weekly pre and post administration of test compound at different doses. At the end of the experimental protocol, the rats were anesthetized with 3% v/v isoflurane inhalation (Cat: R620 veterinary anesthesia machine, RWD life science, San Diego, USA) and were killed by decapitation. The blood was collected to perform biochemical analysis. Several vital organs like heart, kidney, lungs, spleen, and liver were collected for histological analysis to determine whether any pathological changes were caused by the test materials.

5.3.4 Organ coefficient

The organ coefficient of vital organs is performed to analyze the toxic effects of the administered test compounds on various organs, as the changes in their weight are determined. After the experimental animals in each group were killed, and their organs

were dissected and weighed. The organ coefficient of various organs were calculated by using the formulae[495]:

Organ coefficient= [(Weight of the organ (g))/ (Total body weight (g))] X100

5.3.5 Biochemical analysis

The biochemical analysis of various enzymes was performed on the serum using assay kits as directed by the manufacturer. To evaluate the effect of the test compounds on liver, AST (aspartate aminotransferase), ALT (Alanine aminotransferase), and alkaline phosphatase (ALP). Likewise, creatinine (CRE) and CK-MB were also detected as indicators of kidney and heart function.

5.3.6 Statistical analysis

The data were analyzed statistically using the Graph Pad Prism 5.0 software (San Diego, RRID: SCR_002798). The body weight and the amount of food consumed by the rats in each group were evaluated using two-way ANOVA followed by post-hoc analysis. The biochemical parameters and organ coefficients were analyzed statistically by one-way ANOVA followed by Tukey's multiple comparison test. All data in the present study were presented as means and their standard deviations, with p value less than 0.05 being considered statistically significant.

5.4 Methods used for in-vitro photothermal application:

5.4.1 Cell line maintenance:

The mammalian glioblastoma U-87 MG was cultured in DMEM along with FBS (Fetal Bovine Serum) and penicillin–streptomycin solution, grown in a humidified CO_2 incubator at 37 °C.

5.4.2 Pre-Photothermal and Post-Photothermal *in-vitro* cell culture procedure:

A cytotoxicity assay was performed to evaluate the deleterious effects of tin nanocrystals on U-87 MG cells, a type of mammalian glioblastoma. In accordance with the experimental protocol, a predetermined number of cells (10,000) were seeded in each well of a 96-well cell culture plate, which was divided into two groups, one exposed to light and the other kept in darkness, and allowed to adhere overnight. Thereafter, the cells were incubated with various concentrations of Sn nanocrystals, with an incremental progression from 0.5 µg/ml to 100 µg/ml, for a period of 4 hours. Thereafter tin nanocrystals containing medium were discarded, and 100 µl PBS were added into each well of both treated 96 well plate and the selected plate was irradiated with the help of 980 nm laser (power density: 0.83 W/cm^2) for 3 minutes at specific positions, and subsequently, one was kept in the dark condition. After irradiation, PBS was removed from both plates, and a completely fresh medium was added and incubated for the next 20 hours. Finally, the medium was removed, and fresh MTT-containing medium was added into each well, followed by 2 hours of incubation. After incubation, MTT containing medium was removed, and 100 µl DMSO was added into each well, followed by 30 minutes of incubation. The absorbance was taken at 570 nm in a multiplate reader.

5.4.3 Bright field image:

To check the effect of tin nanocrystals on cell morphology, 5×10^5 cells were seeded in a 12-well cell culture plate, followed by treatment of the tin nanocrystals at 50 µg/ml and 100 µg/ml. Further, the cells were irradiated with a laser and images were captured in a phase contrast microscope (EVOS FL live cell imaging system) at 40 X magnification.

5.4.4 FFT weighted Bright field imaging:

The theory of Fourier Transforms is based on the discretization of signals h(t), into the different frequency sinusoids abbreviated as $H(f)$; defined by below equation[496]:

$$H(f) = \int_{-\infty}^{\infty} h(t) e^{2\pi f t}\, dt \; (1a)$$

Where, H is abbreviated as amplitude, f is frequency and $i\ is\ \sqrt{-1}$ and the subsequent inverse transform can be represented by the equation below:

$$h(t) = \int_{-\infty}^{\infty} H(f) e^{2\pi f t}\, df \; (1b)$$

The above equation $(1b)$ is generated in frequency domain from time domain equation$(1a)$. The above transform can also applied to the space as well as position signals by acquiring imaging data.

Furthermore, to deeply understand the phenomenon of cellular and subsequent subcellular processes the Fourier Transform is further extended towards two dimension and subsequent spatial signals are used to understand the signaling processes. The work relied on generating sample signal based on time series data are basically applied to spatial signals. Thus, two-dimensional Fourier Transform, just an extension of equation $(1a)$, can be represented by equation below:

$$H(f_1, f_2) = \int_{-\infty}^{\infty} \int_{-\infty}^{\infty} h(m,n).\, e(2\pi f_1 m).\, e(2\pi f_2\, n)\, dmdn \qquad (1c)$$

Where, f_i are abbreviated as spatial frequencies, and subsequent m and n are represented by spatial coordinated of x-y plane. The subsequent model for discrete Fourier transform (DFT) can be written based on equation[497, 498] $(1c)$ as below:

$$H(n_1, n_2) = \sum_{k1=0}^{M-1} \sum_{k2=0}^{N-1} h(k_1 k_2).e(2\pi i k_1 n_1/M).\ e(2\pi i k_2 n_2/N)\ \ (1c)$$

The Digital Micrograph software, developed by GATAN with version number 3.51.3720.0, is used for the generating FFT weighted bright-field image that resemble the status of live and dead cells mathematically, prior and post photothermal therapy. A 2D Fast Fourier Transform technique is used by opting single cell, prior to Photothermal therapy, and an Inverse Fast Fourier Transform (IFFT) is applied to generate spatial signals G-1(x), G-2(x), and G-3(x) of sine waves that are generated against small discrete spacings within the full width of single cell, abbreviated as x domain. After Photothermal therapy, the process is repeated with 2D FFT and IFFT to create spatial signals G-1'(x), G-2'(x), and G-3'(x) against x domain with no generation of sine waves indicating, weakened signals and poor cell vitality.

5.5 Photothermal efficiency calculation steps for tin nanocrystals:

The photothermal efficiency of tin nanocrystals was computed by adopting previous method[47]. The calculation details are given below:

$$\eta = \frac{hs(T_{max-}T_{amb}) - Q_{dis}}{(1 - 10^{-A_{980}})I} \qquad (1)$$

Where, h, s, T_{max}, T_{min}, A_{980}, I and Q_{dis} are heat transfer coefficient, surface area of the tube, maximum temperature attained by tin nanocrystals (45.3 °C), ambient temperature (24 °C), absorbance of tin nanocrystals at 980 nm, power of 980 nm laser (0.49 W) and heat dissipated by solvent water and tube, respectively.

The θ parameter is introduced for computation of hs, represented by the equation below:

$$\theta = \frac{T - T_{amb}}{T_{max} - T_{amb}} \qquad (2)$$

The tin nanocrystals system time constant is computed by the equation below:

$$t = -\tau_s \ln(\theta) \qquad (3)$$

According to the Figure 4.2c, τ_s is calculated to be 164.4 seconds. Thus, post calculation of time constant hs is computed by the equation below:

$$hs = \frac{mC}{\tau_s} \qquad (4)$$

In above equation m is mass of nanocrystals used for experiment, C is specific heat of aqueous solution of nanocrystal, and τ_s is time constant for the nanocrystal system. Consequently, the value of hs for nanocrystal system is found to be 12.97 mW/°C.

The dissipated heat energy (Q_{dis}) by quartz tube carrying water is computed by independent calculation of time constant, product (hs) of heat transfer coefficient (h) and surface area of tube (s), by using the equation below:

$$Q_{dis} = hs(T_{max} - T_{amb}) \qquad (5)$$

Thus by adopting eq. (5) the value of Q_{dis} is computed to be 68.174 mW. Therefore, the final photothermal efficiency of tin nanocrystals are calculated by eq. (1) to be 42.4%.

5.6. Results and Discussion

5.6.1 Room temperature synthesis of alpha tin nanocrystals with beta phase, as explained through XRD, HR-TEM, and SAED characterizations

The detailed synthesis of ultra-small diamond cubic tin nanocrystals (α-Sn) with beta forms at ambient temperature can be found under 5.3 section. Subsequently, a HR-TEM technique was conducted to ascertain the dimensions of the synthesized tin nanocrystals. Figure 5.1B illustrates, the average size of the tin nanocrystals to be as 4.90 nm (standard deviation~2.30 nm). In addition, the X-ray diffraction (XRD) examination conclusively established the existence of the α-Sn (111) (diamond-cubic, a=6.65596 Å), and β-Sn (020), β-Sn (011) (tetragonal, a=5.83930 Å, c=3.18760 Å) crystal planes, corroborated by matching with the crystallographic open database COD-1512542 and COD-7222460, respectively (Figure 5.1A and Figure 5.2-5.3). Crystallographic open database data of alternative phases, such as pure SnO_2 (COD-5000224) and SnO (COD-4124667) is also compared to rule out their existence (Figure 5.1A and Figure 5.4). This study availed itself of the Fourier-transform technique to appraise the lattice fringes of synthesized Sn nanocrystals, as detected by HR-TEM. Table 1 contains measured and predicted values of the lattice fringes pertaining to the fabrication of tin nanocrystals. The information for the

predicted values of lattice fringes were procured through the utilization of the, COD-1512542, with AMCSD-0011246 for α-Sn, and COD-7222460 with AMCSD-0012875 for β-Sn. (Table 1) The lattice fringes were measured at 0.29 and 0.336 nm, which correspond to the crystal planes (020) and (111) of β-Sn (Figure 5.1C). The lattice fringes were detected at 0.374 and 0.372 nm on additional examination at an alternate selected location in HR-TEM, which corresponds to the crystal plane (111) of α-Sn (Figure 5.1D, E). The transmission electron microscope analysis further confirmed the presence of the (111) crystal plane in β-Sn with a d-spacing of 0.337 nm (Figure 5.1F). The aforementioned estimated lattice fringes of tin nanocrystals were also observed in the experimental XRD peaks of α-Sn (111) and β-Sn (020) (Figure 5.1A and Figure 5.2-5.3). The quantitative assessment of lattice fringes of fabricated tin nanocrystals is also accompanied by employing Selective Area Electron Diffraction (SAED) patterns at two alternate locations via HR-TEM analysis by measuring the diffraction rings pertaining to crystallographic planes of α-Sn (111), α-Sn (202), α-Sn (131), α-Sn (220), α-Sn (331), α-Sn (242) with β-Sn (111), β-Sn (020), β-Sn (011), β-Sn (311) (Table 1) (Figure 5.1G-H). Consequently, aforementioned comparative investigations have revealed that the quantity of crystallographic planes of alpha tin nanocrystals is conspicuously higher when compared with its beta phase. Thereby, the focus of our study is envisioned towards the alpha tin nanocrystals due to their heightened detection frequency on comparison with beta tin crystals, and demonstration of a band gap of 2.38 eV, which closely aligns with the previously estimated band gap of 2.22 eV[297] for alpha tin nanocrystals. Ultimately, the successful synthesis of alpha tin with beta tin nanocrystals at ambient temperature is unequivocally established, based on XRD analysis, HR-TEM, and SAED patterns.

Table 1 The measured values of 'lattice fringes' calculated by Selective area electron diffraction pattern (SAED), High resolution transmission electron microscopy (HRTEM), and High Resolution X- ray diffraction (HR-XRD) analyses. The data for predicted values of lattice fringes were obtained through Crystallography Open Database (COD), COD-1512542, with American Mineralogist Crystal Structure Database (AMCSD), AMCSD-0011246 for α-Sn, and COD-7222460 with AMCSD-0012875 for β-Sn.

Sn Phase(1)	Indexing	Measured Spacing	Predicted Spacing	Sn Phase (2)	Crystal Plane Indexing	Measured Spacing	Predicted Spacing
α-Sn	(111)	0.391(SAED) 0.374(HRTEM) 0.372(HRTEM) 0.384(HRXRD)	0.374(AMCSD) 0.384(COD)	α-Sn	(111)	0.388(SAED) 0.374(HRTEM) 0.372(HRTEM) 0.384(HRXRD)	0.374(AMCSD) 0.384(COD)
β-Sn	(111)	0.336(SAED) 0.337 (HRTEM) 0.336(HRTEM)	0.336(AMCSD)	β-Sn	(111)	0.336 (SAED) 0.337 (HRTEM) 0.336(HRTEM)	0.336(AMCSD)
β-Sn	(020)	0.296(SAED) 0.291(HRXRD)	0.290(AMCSD) 0.291(COD)	β-Sn	(011)	0.270(SAED)	0.279(COD)
β-Sn	(011)	0.264(SAED)	0.279(COD)	α-Sn	(202)	0.234(SAED)	0.235(COD)
α-Sn	(220)	0.228(SAED)	0.229(AMCSD)	α-Sn	(131)	0208(SAED)	0.200(COD)
β-Sn	(311)	0.178(SAED)	0.175(AMCSD)	β-Sn	(311)	0.179(SAED)	0.175(AMCSD)
α-Sn	(331)	0.148(SAED)	0.148(AMCSD)	α-Sn	(331)	0.144(SAED)	0.148(AMCSD)
α-Sn	(242)	0.131(SAED)	0.135(COD)	α-Sn	(242)	0.133(SAED)	0.135(COD)

The above analyses of lattice fringes are far within the threshold limit of systematic error (7.5%), during the measurement of lattice fringes. These small deviations while measurement of lattice fringes are acceptable due to presence of experimental error and deviation at the nanoscale level.[297] Fast Fourier Transform techniques are utilized to compute lattice fringes through HR-TEM images.

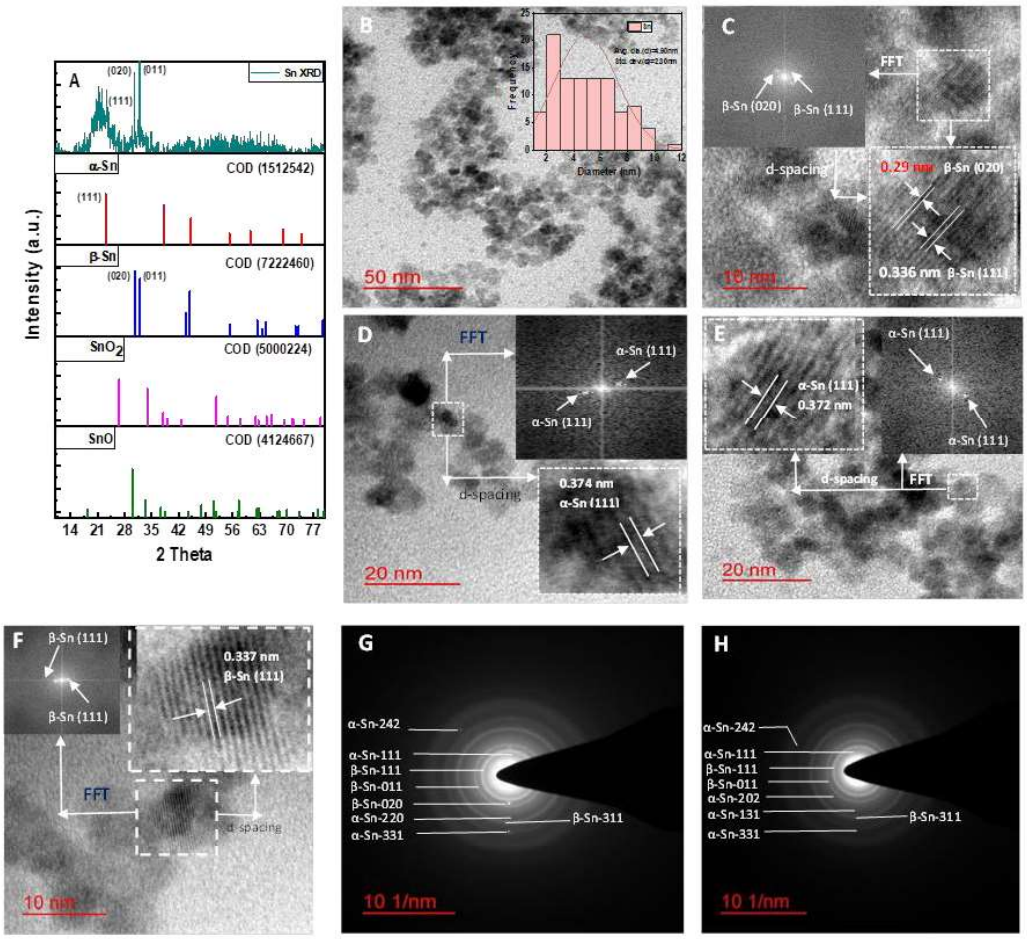

Figure 5.1 (A) The experimental XRD pattern was compared to crystallographic open database (COD) files to confirm formation of α-Sn nanocrystals with β-Sn and to rule out existence of alternative phases, such as SnO_2 and SnO, (B) TEM analysis of ultra-small Sn nanocrystals with an average diameter of 4.90 nm and a standard deviation of 2.30 nm. (C) Using FFT (Fast Fourier Transform), d-spacing values are estimated at 0.336 nm and 0.29 nm, respectively, for β-Sn (111) and β-Sn (020) crystals. (D) FFT (Fast Fourier Transform) estimates d-spacing at 0.374 nm for α-Sn (111) crystals. (E) FFT (Fast Fourier Transform) estimates d-spacing at 0.372 nm for α-Sn (111) crystals. (F) FFT (Fast Fourier Transform) estimates d-spacing at 0.337 nm for β-Sn (111) crystals. (G) Tin nanocrystal formation as revealed by the selective area electron diffraction pattern (SAED). (H) Another selective area electron diffraction pattern (SAED) revealed the formation of tin nanocrystals.

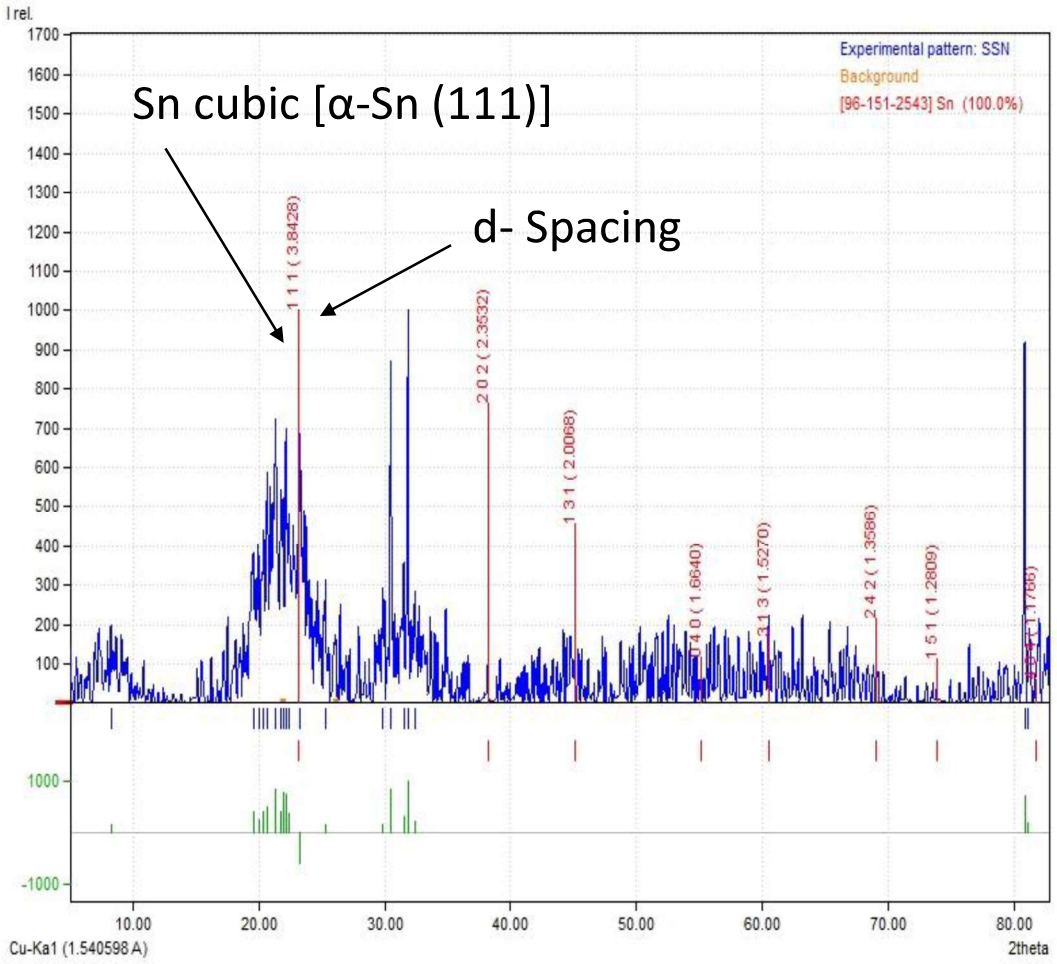

Figure 5.2 Sn cubic α-Sn (111) peak with a d-spacing of 0.384 nm was found in the XRD spectra of Sn nanocrystals (SSN), detected by Match software.

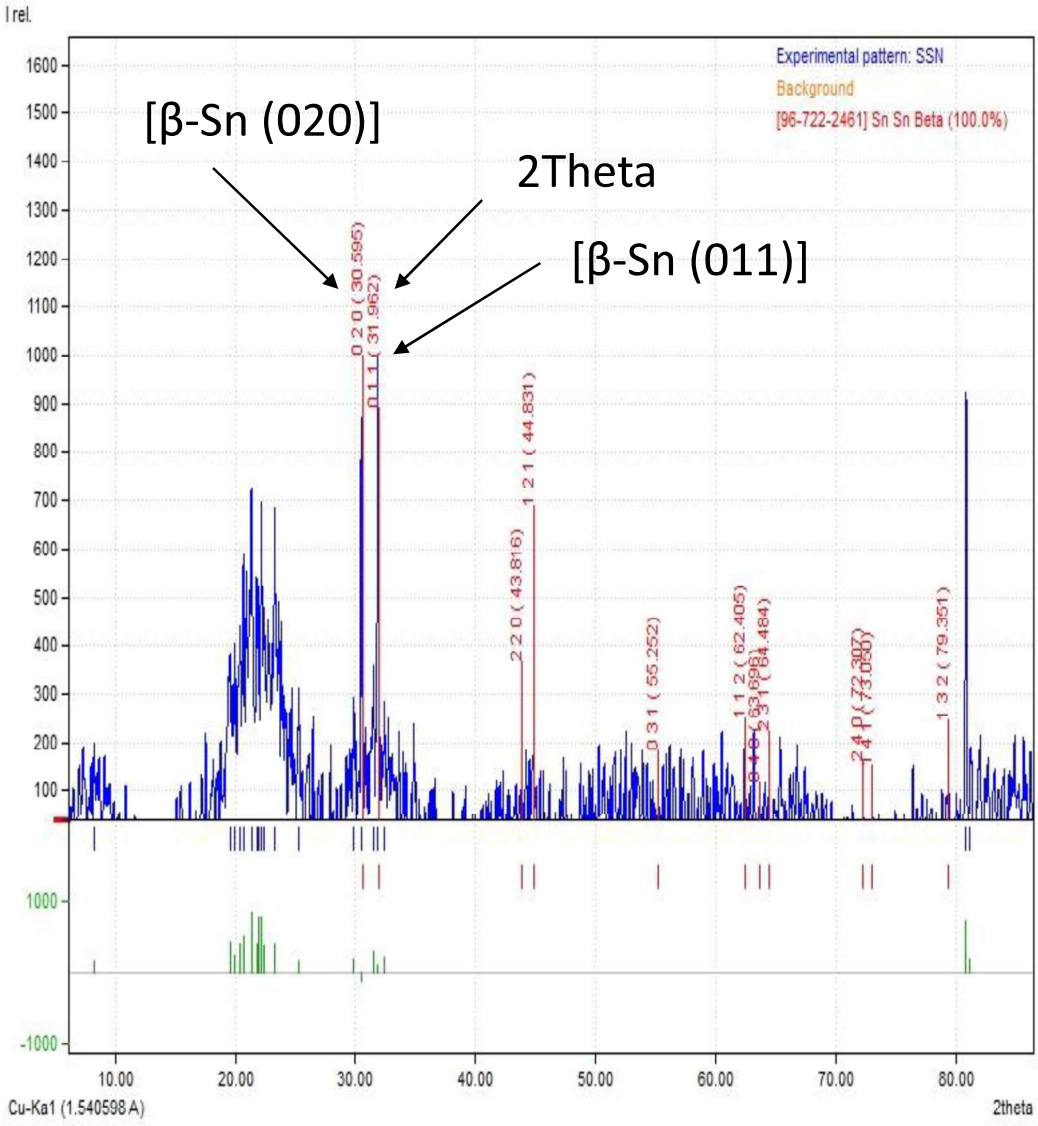

Figure 5.3 Sn tetragonal β-Sn (020) and β-Sn (011) peaks with d-spacing of 0.291 and 0.279 nm was found in the XRD spectra of Sn nanocrystals (SSN), detected by Match software.

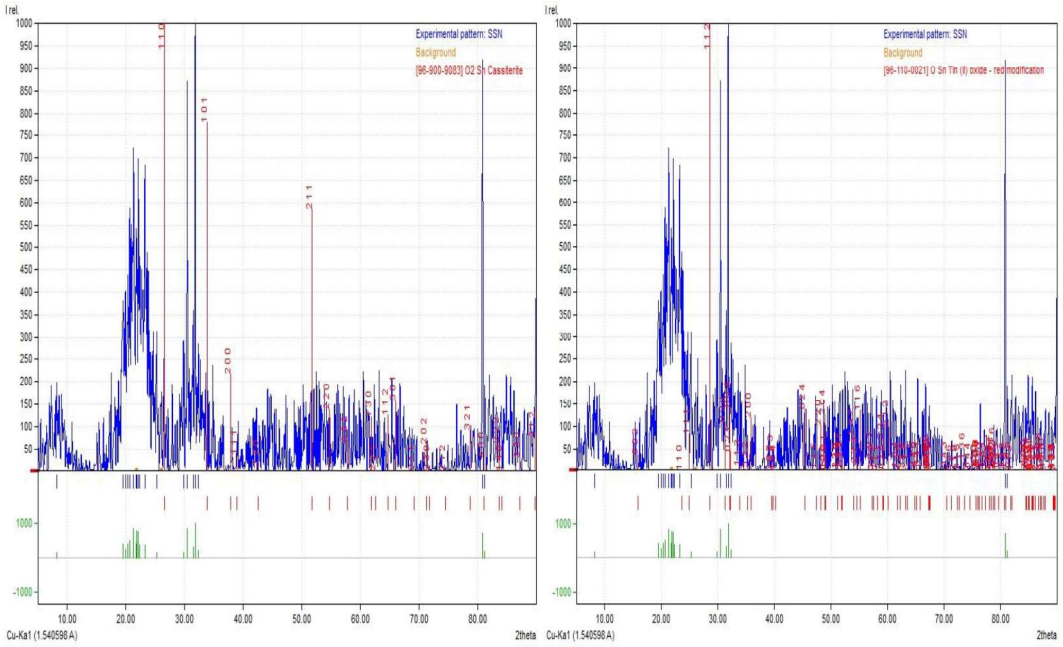

Figure 5.4 No pure SnO_2 and SnO phase peaks were detected by the XRD spectra of Sn nanocrystals (SSN) using Match software.

5.6.2 Inductively coupled plasma mass spectrometry (ICP-MS) analysis and photothermal characterization

Furthermore, ICPMS analysis is employed to ascertain the concentration of tin nanocrystals in solvent water. Standard samples of Sn were used to calibrate the ICPMS, and the results revealed that the concentration of tin nanocrystals in DI water was 1.5816 mg per ml, or 790.8 ppm. (Figure 5.5A–C). Despite the pronounced NIR-II absorbance exhibited by bulk α-Sn, the biomedical application has remained unexplored due to its substantial size (up to 200 nm)[171] and potential alloying with hazardous metals, such as lithium [172], during its synthesis. On the contrary, the bulk synthesis of α-Sn on large substrates (100 nm)[173], makes its use in biology problematic. The current ambient temperature synthesis process yields tin nanocrystals that are both incredibly small and substrate free. This pioneering innovation has led to the very first utilization of such

nanocrystals in the realm of biological sciences. Furthermore, there is immense potential for these substrate free ultra-small tin nanocrystals in several other fields such as lithium ion batteries, the production of electrical devices, superconductivity, and the utilization of diamond cubic alpha tin nanocrystals that resemble properties similar to a 2D layer of graphene.[499] In light of this, the present study has employed the synthesized ultra-small tin nanocrystals (4.90 nm) for biomedical purposes, since nanocrystals smaller than 10 nm are excreted harmlessly by the kidneys[54]. Moreover, the direct band gap of ultra-small tin crystals is determined to be 2.38 eV using a Tauc plot, which is close to the band gap of 2.22 eV for alpha tin nanoparticles calculated by Haq. et al. in 2019[297] (Figure 5.6B). Further, the absorbance properties of tin nanocrystals is studied across a wide range of wavelengths spanning from 200 nm to 1100 nm (Figure 5.6C). In the region of near-infrared light spanning from 800 to 1100 nm, tin nanocrystals exhibit consistently higher absorption values at high concentrations (1.054 mg/ml) compared to lower concentrations (0.790 mg/ml) (Figure 5.5D). The ability to absorb near-infrared light endows tin nanocrystals with remarkable pertinency for use in photothermal applications. Prior exploiting the photothermal attributes of tin nanocrystals for the eradication of malignant cells in an *in-vitro* context, the several concentrations of tin nanocrystals (Q3=1.5816, Q2=1.0544, and Q1=0.7908 mg/ml) in solvent water were exposed to low power density of 980 nm laser (0.83W/cm^2), which resulted in the temperature to rise from 24.0 ℃ to 45.3 ℃ (ΔT=21.3 ℃), 25.9 ℃ to 45 ℃ (ΔT=19.1 ℃), and 24.7 ℃ to 42.5 ℃ (ΔT=17.8 ℃), respectively. Instead, the temperature rise in the irradiated control (water without tin nanocrystals) was just 22.0 °C to 30.9 °C (ΔT=8.9 °C). (Figure 5.6 D) Upon utilizing tin nanocrystals at their maximum concentration of 1.51 mg/ml, a marked elevation in temperature was observed. In merely five minutes, the solution's temperature soared from its initial 24 °C to an impressive 41.3 °C (ΔT=17.3 ℃) (Figure 5.6 D). Next,

the temperature's subsequent plateauing with time elapsed indicates a considerable thermal energy loss.[500] Subsequent synthesis of tin nanocrystals, and over a 7-day period, temperature augmentation remained constant at 45 °C (Figure 5.6E). Furthermore, during a succession of cooling and heating cycles of 180 minutes (3 hrs) duration, an astonishing photostability was exhibited by aqueous solution of tin nanocrystals (Figure 5.6F). Moreover, the outstanding efficiency of ultra-small tin nanocrystals in water is calculated to be 42.4% (Section 5.5), which is substantial higher to the previous calculated photothermal efficiency of Au Nanoshells[46] (15%), Gold nanorods[47] (21.3%), Pt-PEG Nanoworms[48] (38.9%), Pt nanoparticles[49] (22.98-30.88%), Pt cubes[50] (32.3%) and Cys-CuS NPs[47] (38%), Consequently, this nanomaterial possesses all the requisite attributes for utilization in photothermal systems.

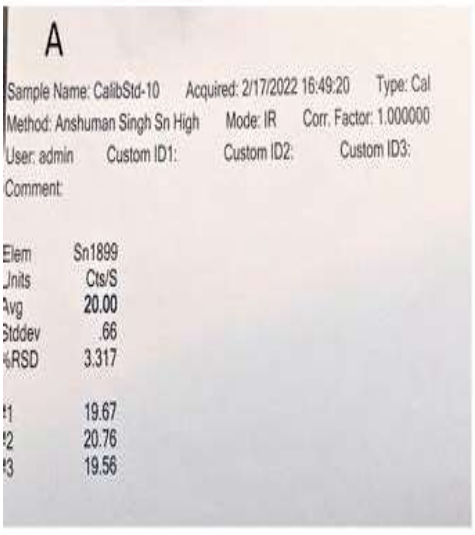
A

Sample Name: CalibStd-10 Acquired: 2/17/2022 16:49:20 Type: Cal
Method: Anshuman Singh Sn High Mode: IR Corr. Factor: 1.000000
User: admin Custom ID1: Custom ID2: Custom ID3:
Comment:

Elem	Sn1899
Units	Cts/S
Avg	20.00
Stddev	.66
%RSD	3.317
#1	19.67
#2	20.76
#3	19.56

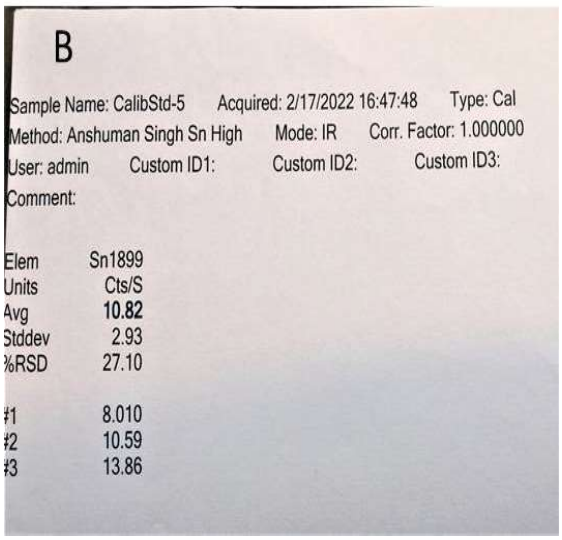
B

Sample Name: CalibStd-5 Acquired: 2/17/2022 16:47:48 Type: Cal
Method: Anshuman Singh Sn High Mode: IR Corr. Factor: 1.000000
User: admin Custom ID1: Custom ID2: Custom ID3:
Comment:

Elem	Sn1899
Units	Cts/S
Avg	10.82
Stddev	2.93
%RSD	27.10
#1	8.010
#2	10.59
#3	13.86

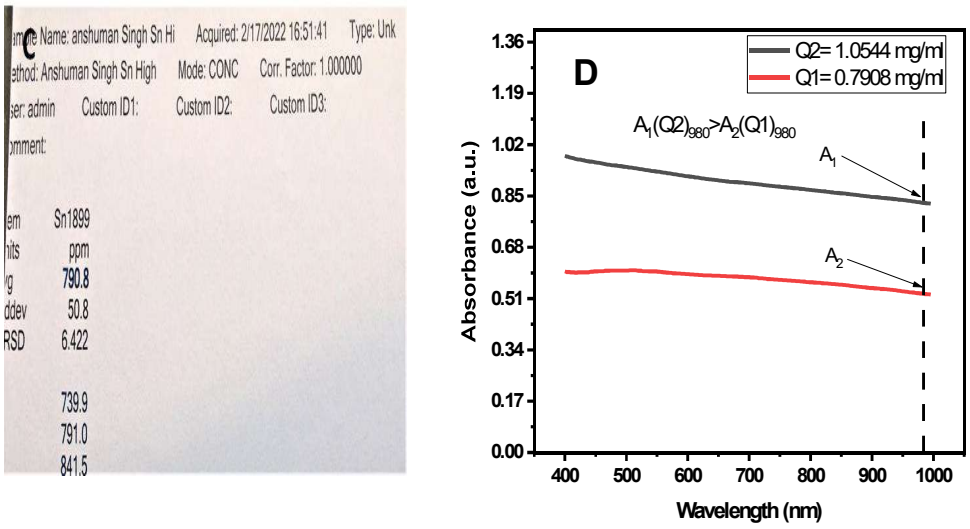

Figure 5.5 (A-B) Calibration standard preparation before acquiring Sn concentration by ICPMS. (C) The measured concentration of synthesized Sn nanocrystals (790.8 ppm) in deionized water by ICPMS. (D) The value of the absorbance (A_1) at high concentration of tin nanocrystal (Q2= 1.0544 mg/ml) is higher when compared to the absorbance value (A_2) at the low concentration of tin nanocrystal (Q1=0.7908 mg/ml) at the specific 980 nm wavelength.

Subsequently, the MTT assay was executed using a standard procedure to ascertain the toxic impact of tin nanocrystals. The obtained result shows that irradiation to the cells (980 nm CW laser) at 25 µg/ml, 50 µg/ml and 100 µg/ml concentration of tin nanocrystals, significantly induce toxicity and inhibit cell growth as compared to without irradiated cells (Figure 5.6I). At the highest concentration of tin nanocrystals (100 µg/ml), the cell viability was found to be only at 36.38%. Therefore, on the basis of obtained results it can be inferred that irradiation of cells in the presence of tin nanocrystals acting as a catalyst that is promoting cell death.

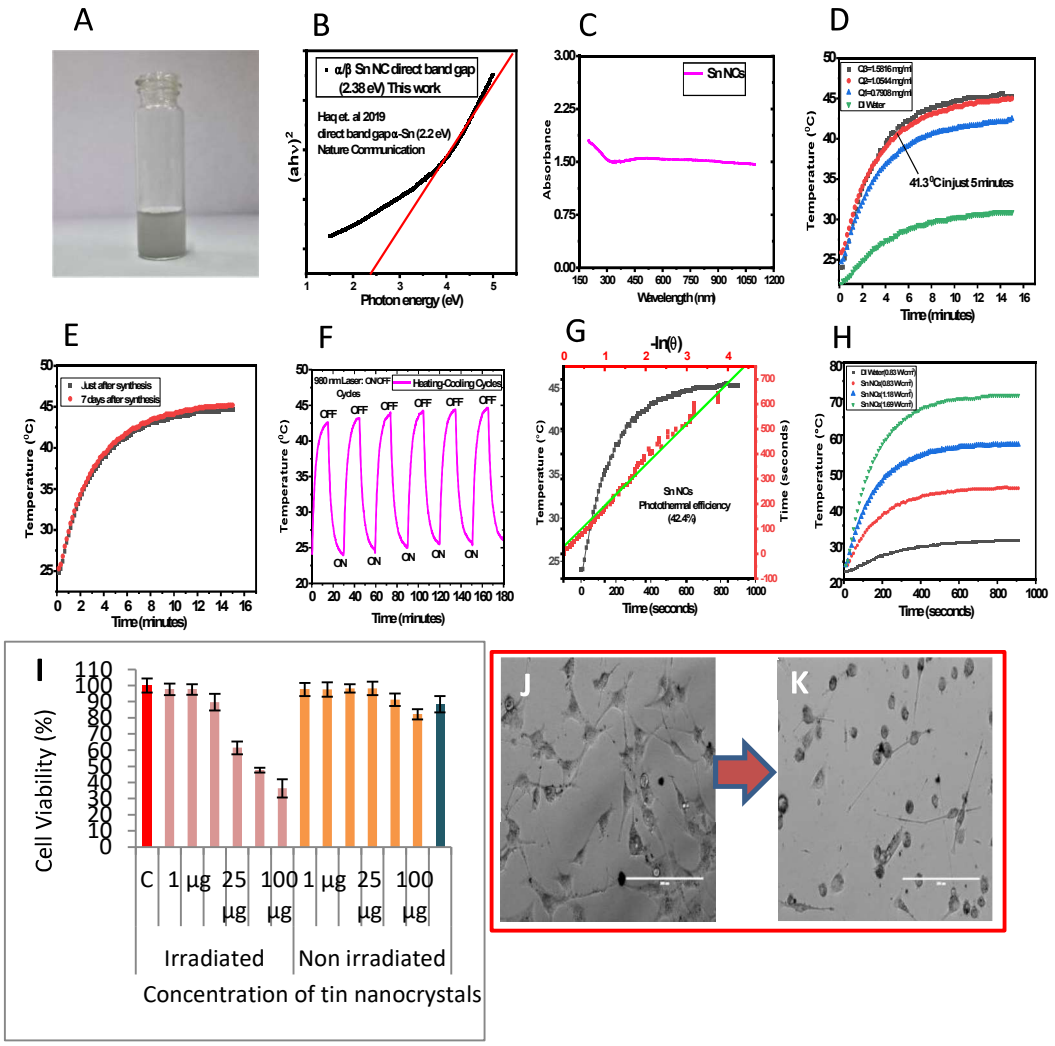

Figure 5.6 (A) Synthesized tin nanocrystals in water as aqueous solution. (B) Direct band gap of tin nanocrystals is estimated to be 2.38 eV, close to alpha tin nanocrystals (2.2 eV). (C) The absorbance spectra of tin nanocrystals over a wide wavelength range between 200 nm and 1100 nm. (D) Temperature vs time spectra for tin nanocrystals at concentration of 1.5816 mg/ml and corresponding efficiency calculation by $-ln(\theta)$ ***vs time*** plot (E) Time-dependent temperature rise in an aqueous solution of 1.5816 mg/ml tin nanocrystals, compared to water as a control subjected to irradiation at several laser power densities (0.83, 1.18 and 1.69 W/cm^2). (F) The time-dependent temperature rise in tin nanocrystal aqueous dispersion when concentration was increased from 0.7908 to 1.58 mg/ml. (G) The increase in photothermal temperature is continuous after synthesis and over the next seven days. (H) A remarkable photothermal stability at 980 nm laser wavelength over 180 minutes of heating and cooling cycles. (I) Tin nanocrystals at various concentrations was subjected to an MTT test after and before being exposed to a 980 nm laser. (J) Bright-field image shows cells with 110 µg/ml tin nanocrystals, as well as the morphology of cells both before and after being irradiated by a 980 nm laser.

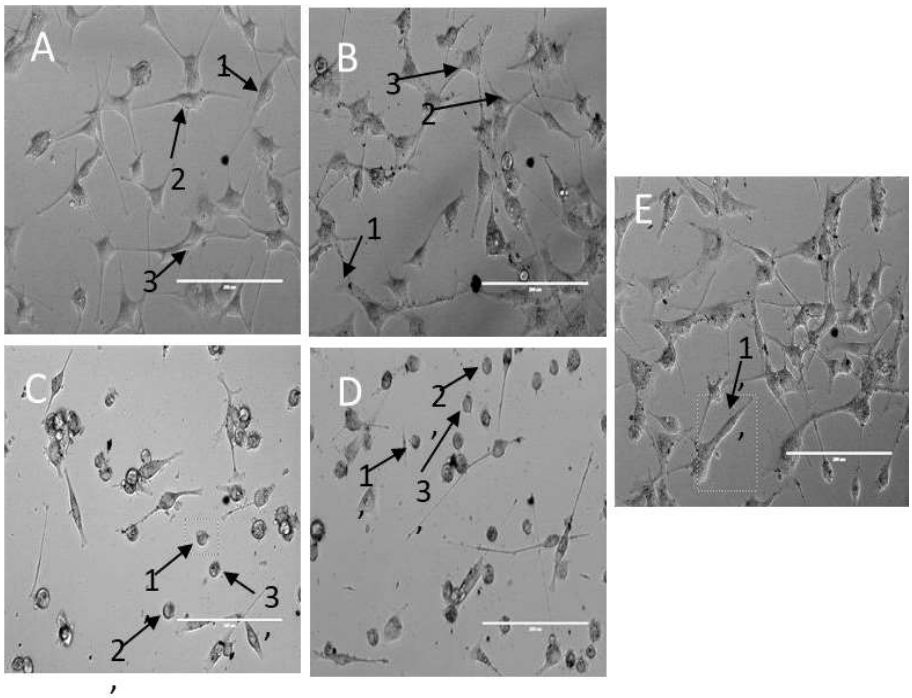

Figure 5.7 (A-B) Bright-field image: The morphology of cells before irradiation by laser with varying tin nanocrystal concentrations, with 110 µg/ml and 50 µg/ml tin nanocrystals, respectively, and 1, 2, and 3 pointed cells selected for FFT analysis. (C-D) The morphology of cells after being irradiated by a 980 nm laser, and 1', 2', and 3' pointed cells selected for FFT analysis. (E) The morphology of control cells carrying culture media with 1'' pointed cell was chosen for FFT imaging analysis,

5.6.3 Fast Fourier Transform (FFT) weighted Bright Field Imaging

Using the bright field image, a complete spectrogram is generated by taking two-dimensional FFT of signal cells carrying tin nanocrystals (Figure 5.7). The spectrogram's intensity ranges from 0 to 100, where 0 scale intensity represents dead cells and 100 scale intensity represents cells with eminent cell viability. Morphological analysis is performed to determine cell vitality. When the color in spectrogram of single cell changes from red to blue to green and final to orange, the cell viability decreases in same pattern.

Subsequently, the technique of Fast Fourier Transform (FFT) weighted bright field imaging was employed via single cell spectrogram, on the scale of 0 to 100, to prognosticate the cellular response to the photothermal therapy prior to and subsequent to its application, as *in-vitro*. (Figure 5.9) A control that retains cells with culture media, displaying 100% viability as determined by MTT assay, as exemplified in the bright field image with 1'' pointed single cell morphology, was selected as the reference for FFT

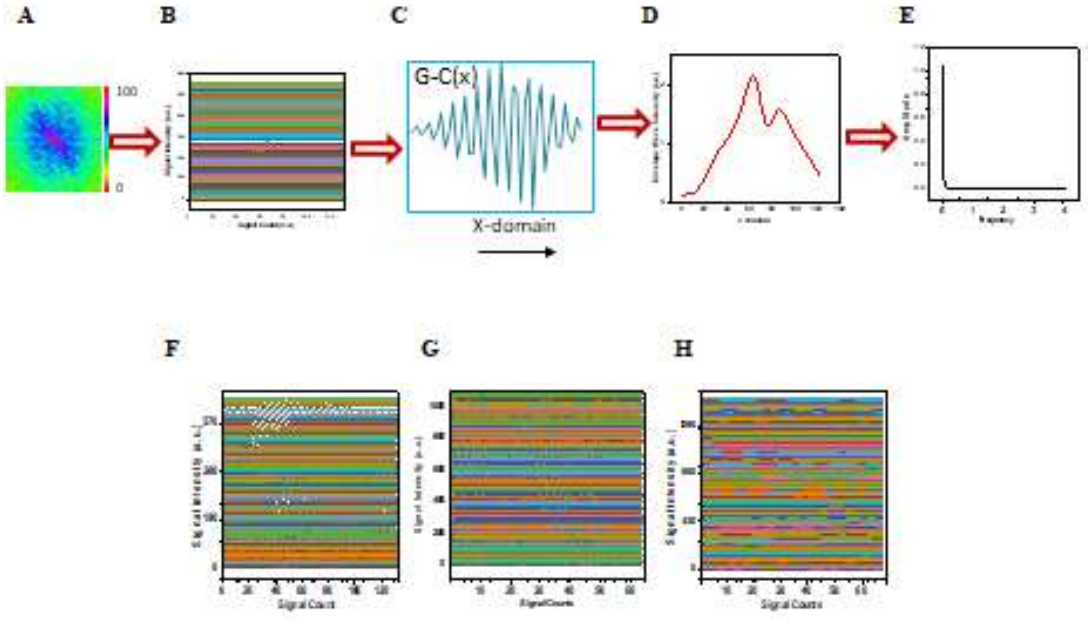

Figure 5.8 (A) FFT Spectrogram for selected control cell (B) 2D signals generated through IFFT for control cell (C) G-C(x) is one dimensional amplitude modulated wave signal generated through 2D IFFT signal in x domain for the control cell. (D) Enveloped wave signal generated through amplitude modulated wave signal (E) Amplitude vs Frequency signal generated through FFT of amplitude modulated wave (F-H) 2D signals generated through IFFT of selected cell (1,2, and 3 pointed morphology) carrying Sn NCs (110 μg/ml).

imaging analysis (Figure 5.8). Prior to the therapeutic intervention via 980 nm laser, the bright field image exhibited cells displaying 1, 2, and 3 pointed morphologies with tin nanocrystals concentrations of 110 and 50 µg/ml. (Figure 5.7 A-E) At a concentration of 110 µg/ml of tin nanocrystals, the live malignant cells induced amplitude modulated wave signals in the x domain, as evinced by G-1(x), G-2(x), and G-3(x) functions, which were subsequently utilized to extract the final sinusoidal enveloped wave signal (Figure 5.9 A-C). Moreover, pre-photothermal therapy, the single cell FFT analysis in the green channel and its subsequent spectrogram manifested green, red and blue coloration (100% strength; eminent cell vitality), respectively, implying the strength of the enveloped sine waveform signal. Furthermore, the subsequent 1-D FFT analysis yielded amplitude vs frequency spectra (Figure 5.9C-E). Subsequently, post-photothermal therapy, the bright field imaging revealed the persistence of malignant cells displaying 1', 2', and 3' pointed morphologies. (Figure 5.7C-D) Nonetheless, the FFT analysis of such cells indicated the absence of amplitude modulated waveform signals in the x domain, as evinced by G-1'(x), G-2'(x), and G-3'(x) functions. The utilization of the FFT in the green channel and its corresponding spectrogram depicted black and orange coloration, respectively, indicating a diminution in amplitude modulated wave signal intensity for three individual cells, as a a null waveform signal (0% signal strength; cell death) was designated as such (Figure 5.9F-H). The photothermal damage to the malignant cells is in accordance with the strength of envelope wave signal, which diminished from red (100% strength; cell vitality) to blue, and ultimately to orange coloration (0% strength; cell death) in the spectrogram of single cell. These fluctuations in the strength of the envelope signal pre and post photothermal are proportionate to alterations in the morphology of the malignant cells. The proposed mathematical models and parameters, pre and post photothermal therapy are presented in the Table 2.

Table 2 containing fitted sine wave parameters for control and selected cells, carrying Sn NCs (110 µg/ml), Pre-photothermal.

Cell Number	Y_0	X_C	W	A*	Adjusted coefficient of determination
Control (1")	0.91074±0.0710	33.37985±2.772	72.6391±5.0588	**0.84642±0.0583**	0.99
Malignant cell (1)	0.4260±0.02912	201.31119±12.6367	294.71013±24.3861	**0.34709±0.0341 5**	0.99
Malignant cell (2)	0.52973±0.02661	344.28628±10.4392 7	364.10464±11.722	**0.47249±0.0370 9**	0.99
Malignant cell (3)	1.41596±0.040	199.8677±3.54	225.72334±3.7	**1.4146±0.0568**	0.99

*During, pre-photothermal therapy the amplitude of enveloped wave signals generated through cells carrying Sn NCs are found to be approximately of same amplitude when compared to enveloped wave signals generated through control cells, carrying culture media. Thereby, during pre- photothermal therapy, this proposed model can best predict the cell vitality mathematically, based on wave pattern of control group.

5.6.4 The predicted model pre-photothermal operation acquainted by FFT approach:

The simulation of FFT weighted imaging was also replicated utilizing an alternate concentration of tin nanocrystals (50 µg/ml), both antecedent to and succeeding photothermal therapy (Figure 5.9I-J). Prior to the photothermal therapy, the cellular signals emanating from cells containing tin nanocrystals were observed to be analogous to those of the control group. Consequently, a prognostic mathematical model was formulated, demonstrating that the presence of a waveform signal is an indicator of cell viability, whereas its absence subsequent to photothermal therapy (as corroborated by MTT assay and a control group) intimates cell demise. The aforementioned mathematical model of the envelope wave signal, pre-photothermal, can be expressed using equation below:

$$y = y_0 + Asin\left(\pi \frac{x - x_c}{w}\right)$$

Where, the value of fitted parameters are y_0 , x_c, w, and A, which are abbreviated as, offset, phase shift, period, and amplitude of the envelope wave signal chosen generated through cells carrying Sn NCs (110 μg/ml), respectively. These parameters values are shown in Table 2. Post photothermal therapy, null waveform is detected through spectrogram of single cells, resulting in existence of flattened signal with no amplitude, implying cell demise. These flattened signal can be represented mathematically by equation by $y = c$, where y is output and c is arbitrary constant.

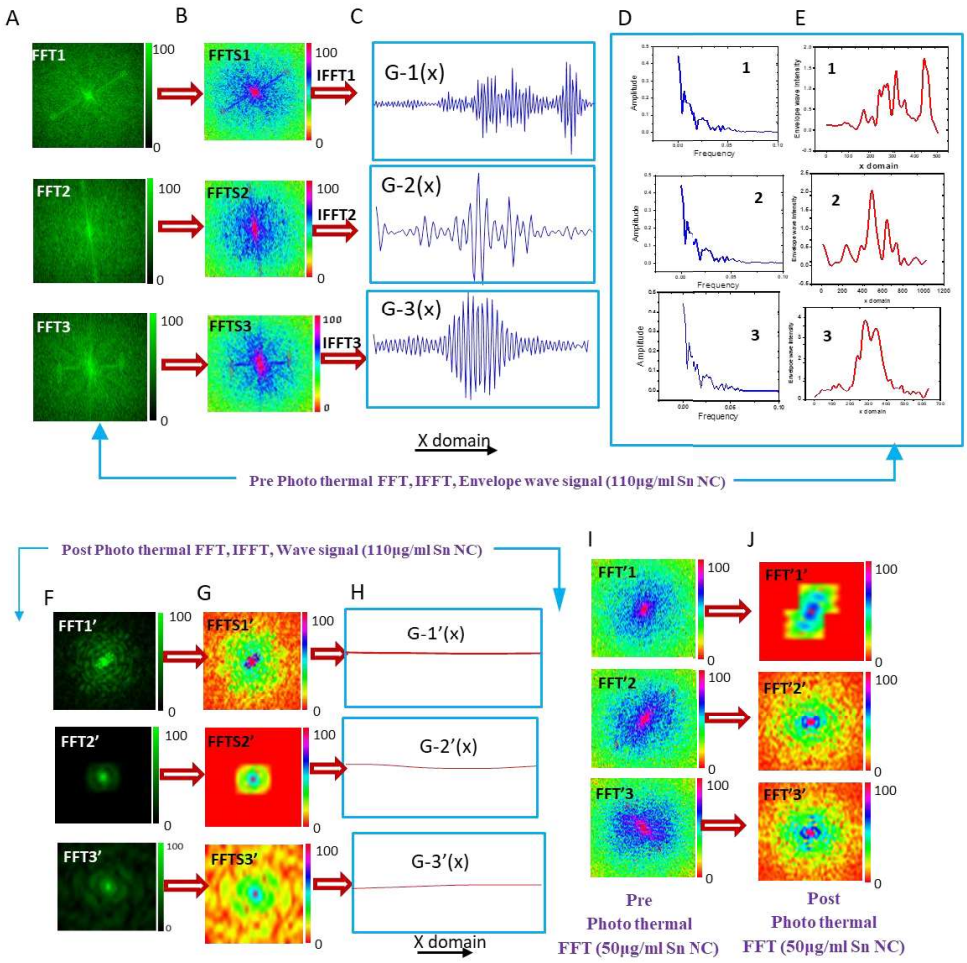

Figure 5.9 Fast Fourier Transform weighted single cell Bright-field imaging: Pre-Photothermal (A) FFTG-2D FFT Spectrum in green channel on 3 selected cells with 110 µg/ml Sn NC. (B) FFTS-2D FFT spectrogram carrying 110 µg/ml Sn NC on three individual cells (C) IFFT extracted amplitude modulated wave signal G-1(x), G-2(x) & G-3(x) under x domain. (D) Extraction of envelope wave signal from amplitude modulated wave (E) Amplitude vs frequency signal extracted from envelope wave signal. Post-Photothermal: (F) FFTG-2D FFT Spectrum in green channel on 3 selected cells with 110 µg/ml Sn NCs. (G) FFTS-2D FFT spectrogram carrying 110 µg/ml Sn NCs on three individual cells. (H) G-1(x), G-2(x) & G-3(x) signals diminishes after photothermal treatment. (I-J) FFTS-2D FFT spectrogram carrying 50 µg/ml Sn NC on three individual cells before and after photothermal.

5.6.5 Biocompatibility assessment of tin nanocrystals within the Wister Rats

The *in-vivo* acute tail vein toxicity assessment of tin nanocrystals was conducted on four groups of healthy adult male Wistar rats, with six rats being allocated to each group, wherein different concentrations of tin nanocrystals (Q1, Q2 and Q3) were administered at a dose of 17.5 mg/kg body weight. Table 3 shows general behavioral and observation analysis in Wistar rats, for the first 4 hrs and during 14 days of administration of the tail-vein injection. The results indicate that no deaths were recorded at any of the administered doses within the initial 4-hour timeframe or during the 14-day observation period. Subsequently, rats exhibited no signs of toxicity, such as changes in fur, respiratory mucosa, skin, fatalities, somatosensory discomfort, or circulation during a 14-day observation period, after administering a single dose of different concentrations of tin nanocrystals. (Table 3) In addition, rats injected with tin nanocrystals exhibited no behavioral abnormalities, such as tremors, salivation, or convulsions. (Table 3) Furthermore, intravenous injection of tin nanocrystals had no effect on the morphology of essential organs, such as the heart, kidneys, lungs, spleen and liver (Figure 5.10A-E). Weight fluctuations and organ coefficient analyses in Wistar rats are provided under section 5.6.6 and 5.3.4. Due to the aforementioned findings, it is regarded safe to employ tin nanocrystals in a number of biological applications.

Table 3 General behavioral and observation analysis for the first 4 hrs. and during 14 days after single-dose administration of different concentrations of tin nanocrystals (Q1=0.7908 mg/ml, Q2= 1.0544 mg/ml and Q3= 1.5816 mg/ml) in rats (n = 6 male rats/group).

General behavioral and observation analysis	Control		Sn NCs (Q3)		Sn NCs (Q2)		Sn NCs (Q1)	
	4hrs	14 days	4hrs	14 days	4hrs	14 days	4hrs	14 days
Eyes	UC	UC	UC	UC	UC	UC	UC	UC
Skin and Fur	UC	UC	UC	UC	UC	UC	UC	UC
Salivation	UC	UC	UC	UC	UC	UC	UC	UC
Mucous Membrane	UC	UC	UC	UC	UC	UC	UC	UC
Diarrhea	NO	NO	NO	NO	NO	NO	NO	NO
Sleep	N	N	N	N	N	N	N	N
Lethargy	NO	NO	NO	NO	NO	NO	NO	NO
Tremors & Convulsions	NO	NO	NO	NO	NO	NO	NO	NO
Coma	NO	NO	NO	NO	NO	NO	NO	NO
Behavior and somatosensory activity	N	N	N	N	N	N	N	N
Consistency and color of faces	N	N	N	N	N	N	N	N

Note: NO-Not observed N-Normal, and UC-Unchanged.

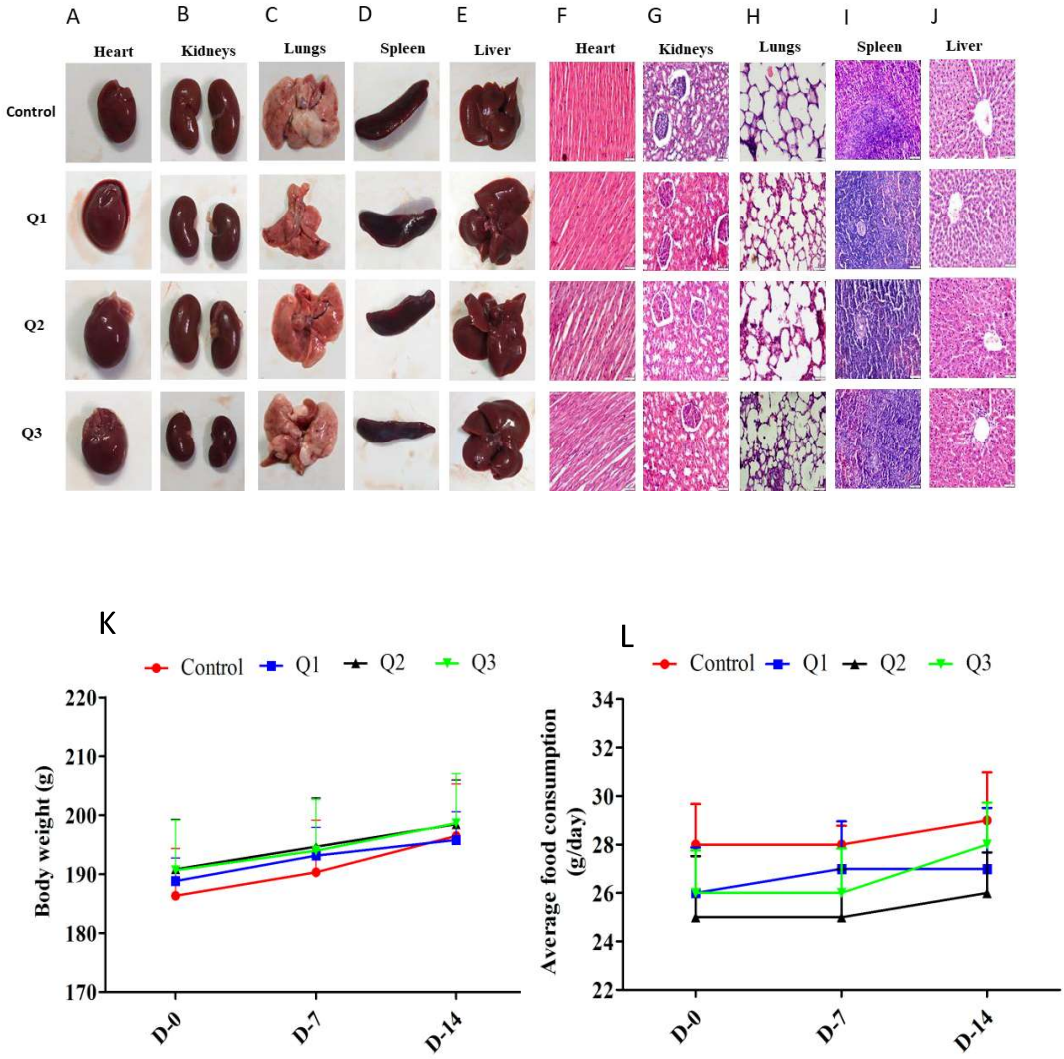

Figure 5.10 (A-E) Typical photographs that exhibit the normal morphology of Heart, Kidneys, Lungs, Spleen, Liver treated rats after single-dose intravenous administration of Sn nanocrystals at concentrations of Q_1=0.7908 mg/ml, Q_2= 1.0544 and Q_3= 1.5816 mg/ml. (F-J) Effect of single dose intravenous administration of Sn nanocrystals at concentrations of Q_1=0.7908 mg/ml, Q_2= 1.0544 and Q_3= 1.5816 mg/ml on highly perfused organs like Heart, Kidneys, Lungs, Spleen, Liver , stained with eosin and hematoxylin, showcasing the intricate structures within. (K-L) Effect of single dose intravenous administration of different concentrations of tin nanocrystals on body weight and average food consumption at various intervals during 14 days of the experimental protocol. All values are displayed as mean±SD (n=6 male rat/group). (A statistical analysis method consisting of a two-way analysis of variance, followed by Bonferroni post hoc test/ 6 times experiment repeated).

5.6.6 Weight fluctuation in Wistar RATS during tail vein administration of tin nanocrystals:

Weight fluctuations in test animals are often used as a proxy for healthy organ function. Animals' physiological responses to test materials are widely accepted as valid indicators of inflammation, abrasion, or impending mortality.[501] Figure 5.10K displays the results of regular measurements taken of the rats' body weights during the present preclinical toxicity evaluation. Two-way analysis of variance (ANOVA) revealed no statistically significant differences in body weight among groups ([$F(3,60)= 0.8933$; $p>0.05$]), across time ([$F(2,60)= 6.969$; $p>0.05$), or as a result of their interaction ([$F(6,60)= 0.07263$; $p>0.05$). Also, there were no noteworthy discrepancies in the amount of food or drink consumed by the groups during the course of the trial (Figure 5.10L). As a result, tin nanocrystals may be confidently said to be safe for therapeutic usage and not harmful.

5.6.7 Organ Coefficient in Wistar RATS during tail vein administration of tin nanocrystals:

The organ coefficient, which quantifies the alteration in organ weight, is a crucial aspect of toxicity evaluation, as it is often an early indicator of organ toxicity. Therefore, measuring it during toxicological analysis of any novel synthesized compounds is imperative.[502] Figure 5.11(A-E) illustrates the single-dose effect during tail vein administration of tin nanocrystals on the organ coefficients related to vital organs (heart, kidneys, lungs, spleen, and liver) during the process of acute toxicity study. Statistical analysis based on one-way ANOVA revealed, no existence of any significant differences in the organ coefficients of vital organs i.e., heart, kidneys, lungs, spleen, and liver ([$F(3,23)=0.1278$;$p>0.05$], [$F(3,23)=0.9348$;$p>0.05$], [$F(3,23)=1.904$;$p>0.05$], ([$F(3,23)= 2.417$; $p>0.05$]), and ([$F(3,23)= 0.7376$;$p>0.05$) respectively (Figure 5.11A-E). This

confirms that single dose administration of tin nanocrystals did not have any toxicological effects on highly perfused organs which also corroborates with the histological analysis data of these organs (Figure 5.10F-J).

5.6.8 Biocompatibility assessment on intravenously injected tin nanocrystals through histopathological and blood serum enzyme assessments

In the assessment of the safety profile of exogenous substances administered systemically, it is customary to conduct histopathological investigations[503]. In Figure 5.10F-J, rats treated with a single dose of tin nanocrystals exhibited intact architecture without either changes in the histo-architecture of highly perfused organs. The histological slices of hearts in all the groups exhibited that cardiomyocytes are uniformly structured having single, oval, and central placed nucleus with myofibrillary fibres uniformly arranged. Likewise, the treated rats revealed normal myocardial muscle bundles surrounded by thin fibrous collagenous stroma as in the control rats, in accord with stable CK-MB concentrations in serum. (Figure 5.10 F) Similarly, kidney's function is to expel the metabolic wastes from the body and is also responsible for maintaining ionic concentration by absorbing and secreting them into urine through specialized ion channels and transporters[504]. Hence, when screening the tin nanocrystals acute toxicity, it is imperative to consider the effect of tin nanocrystals on the kidneys. The kidneys of both the treated and control groups showed normal-shaped renal tubules. Additionally, the tin nanocrystals treated rats had normally shaped glomerulus, renal and bowman's capsules as seen in the control rats (Figure 5.10G). Also, both in the treated and control groups, histopathologic examination of the lungs revealed no signs of hemorrhage, edema, or fibrosis. Furthermore, the interstitium is free from inflammation, and the alveoli are normal. (Figure 5.10H) Spleen is the most important auxiliary lymphoid organ involved in the elimination of exogenous compounds by phagocytosis once they enter

into the systemic circulation. It has two distinguishing structures i.e., white and red pulp involved in blood filtering and initiation of immune response respectively.[505] Upon intravenous administration of tin nanocrystals, histological examination of the spleen at the end of experimental protocol revealed normal white pulp lymphatic nodules, red pulp splenic cords, and trabecular spleens. (Figure 5.10I) Histological analysis of the sections of rats administered with tin nanocrystals exhibited normal haepatocytes with vesicular nuclei surrounding the central vein. Furthermore, the sinusoids remained unchanged and are comparable to the control groups, suggesting that tin nanocrystals administered to rats did not cause liver damage (Figure 5.10J).

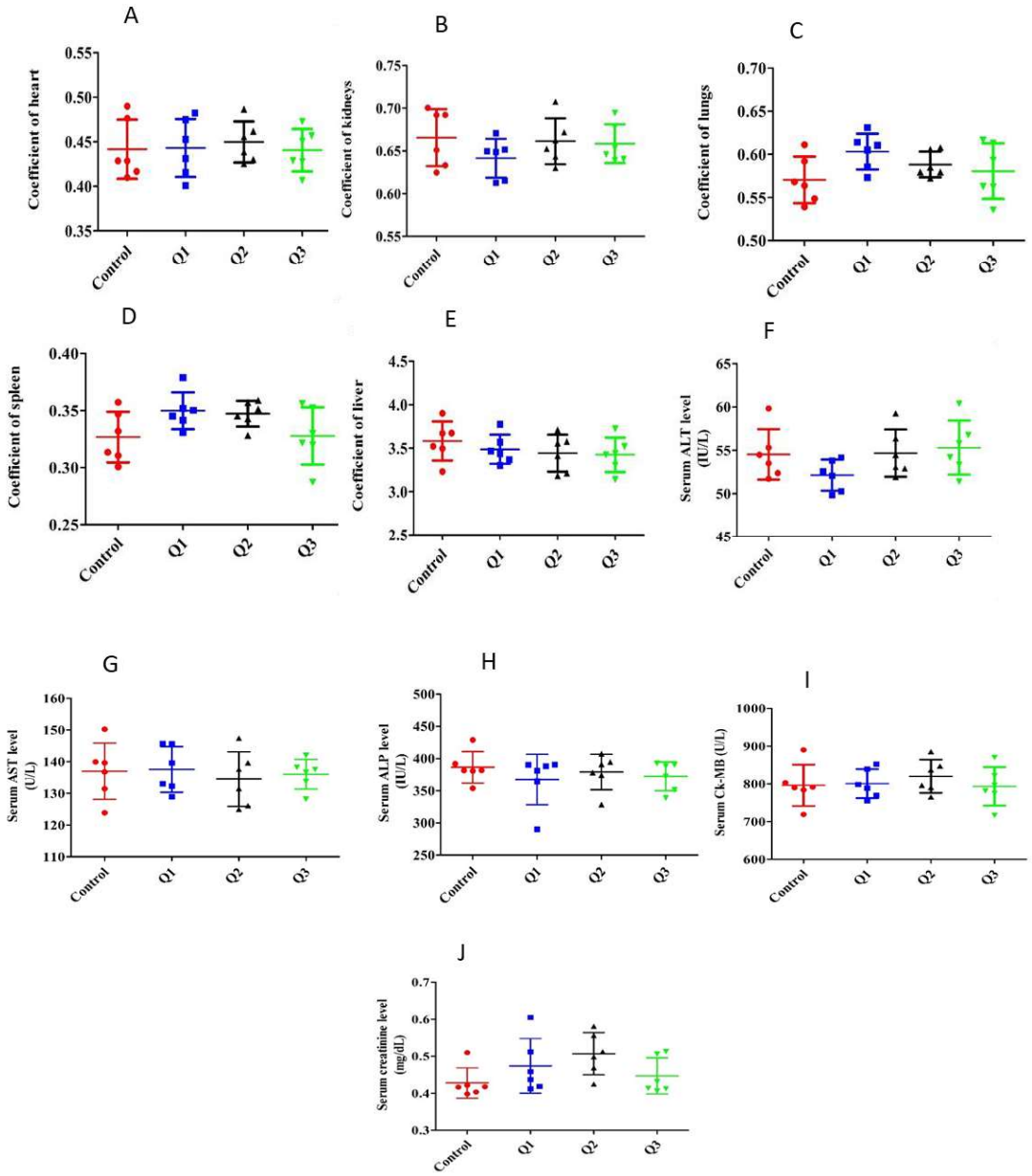

Figure 5.11 (A-E) Effect of single dose intravenous administration of Sn nanocrystals on organ coefficient of Heart, Kidneys, Lungs, Spleen, Liver after end of experimental protocol. All values are displayed as mean±SD (n=6 male rat/group). (One-way ANOVA, followed by Turkey's multiple comparison post hoc test). (F-J) Effect of single dose intravenous administration of Sn nanocrystals on serum concentration of Heart, Kidneys, Liver, Lungs, after end of experimental protocol. All values are displayed as mean±SD (n=6 male rat/group). (One-way ANOVA, followed by Turkey's multiple comparison post hoc test/ 6 times experiment repeated).

Furthermore, the present study also evaluated the potential toxic effects of tin nanocrystals on vital organs by measuring, organ coefficients, ALT, AST, ALP, CK-MB, and creatinine, in the serum at the end of experimental protocol (Figure 5.11A-J). The statistical analysis of organ coefficients are discussed under section 5.6.7. Subsequently, the enzymes are often clinically measured to access the status of organ functioning. Normally, the vital organs (i.e., liver and kidneys) mitigate the toxic load in the body by eliminating the metabolites produced.[495] Therefore, it is crucial to monitor the liver and kidney function during any toxicological studies, since these organs are primarily affected. Clinically, ALT, AST, and ALP are utilized to assess liver function as elevations in AST levels signify hepatocellular necrosis, while changes in ALT levels indicate hepatocyte hypertrophy or other liver-related issues.[506] On the other hand, changes in ALP reflect bile duct congestion.[495] The statistical analysis by one-way ANOVA revealed no significant variations in the serum level of ALT, AST, and ALP levels among the groups ([$F(3,23)= 1.620; p>0.05$], [$F(3,23)=0.1840; p>0.05$], and [$F(3,23)= 0.4857; p>0.05$] (Figure 5.11F-H). Similarly, an anthropometric indicator of the kidney functioning, creatinine changes in the event of kidney damage leading to nitrogenous waste accumulation in the bloodstream, resulting in azotemia.[507] Hence, analysis of serum creatinine level was performed in our study (Figure 5.11J) and there was no statistically significant changes in serum creatinine levels between the groups [$F(3,23)= 2.222; p>0.05$] (Figure 5.11J) Therefore, tail vein administration of tin nanocrystals during the single-dose acute toxicity study revealed no adverse effects on the liver and kidneys.

Further, another vital organ is heart as it pumps blood throughout the body and therefore it is essential to evaluate its functioning post the *in-vivo* administration of test compounds. If there are any toxic reaction on the cardiac tissues there is elevation in CK-MB level in blood[508]. Hence, serum CK-MB level assessment was performed in the present study

as shown in Figure 5.11I. Based on one-way ANOVA statistical analysis, no significant differences were observed between the groups in CK-MB serum levels [$F(3,23)= 0.3863; p>0.05$]. As a result, it can be concluded that tin nanocrystals did not cause any toxicological effects on the cardiac muscle, which is in line with the heart's histoarchitecture (Figure 5.10F-J). This conclusion is further supported by histopathological investigation, as performed earlier (Figure 5.10F-J). Hence, it can be attested that tin nanocrystals are of non-toxic nature and can be further used for various potential biomedical applications.

The present study entails a noteworthy global challenge that addresses the synthesis of alpha tin nanocrystals in their substrate-free form along with their beta counterparts, at ambient temperature. The reduction chemistry is utilized to create ultra-small free-standing tin nanocrystals, which are then employed at the interface of engineering and biology, utilizing sophisticated mathematical modeling through FFT, *in-vivo* toxicological assessments in Wistar rats, and *in-vitro* photothermal analyses, which have never been conducted before. The rapid disclosure of the substrate-free tin nanocrystals fabrication process is expected to have extensive implications not only in the realm of biological applications, but also in various other domains, such as superconductivity, the development of layered films similar to graphene materials, lithium-ion batteries and so on. Thereby, this innovation for synthesizing substrate-free alpha tin nanocrystals in solvent water at ambient temperature marks a significant achievement. These nanocrystals diminutive size, has allowed them to be used for the first time in biological applications. This straightforward, one-pot synthesis technique offers a promising avenue for unlocking their tremendous potential in the impending future.

Conclusion

We report a remarkable finding in the field of semiconducting materials, as we unveil an innovation through electron-hole coupling mechanism for synthesizing room-temperature stable, non-toxic, ultra-small free-standing diamond-cubic tin nanocrystals (α-Sn) with beta forms in the aqueous phase that addresses critical challenges faced by traditional methodologies. For example, traditional approaches often rely on toxic materials such as lithium and lead-telluride, or require bulky reactive substrates like Si/InSb, along with high temperatures (1400°C), and also involve synthesis complexity, high cost to stabilize α-Sn above 13 °C. In contrast, our synthesis approach eliminates the need for such hazardous materials, bulky substrates and elevated temperatures, offering a safer, low cost and more sustainable alternative. Thus, we believe that our work meets the criteria as an urgent communication of vital significance.

We have created an impressive mathematical model through advanced FFT weighted bright field imaging to predict how live cancer cells will respond to photothermal treatment. In-vivo experiments on Wister-rats, followed by a reliable MTT assay, have provided conclusive evidence that tin nanocrystals non-toxic and biocompatible

Notably, these incredibly tiny nanocrystals are truly exceptional! They have an amazing quality to absorb near-infrared (NIR) light and convert it into heat with remarkable efficiency, up to 42.4%! This makes them a valuable asset in the fight against cancer, particularly for treating cancer cells upon shining low power (0.5 W), 980 nm NIR-light (CW-laser).